

Ultra-cold Neutron Production in Anti-ferromagnetic Oxygen Solid

C.-Y. Liu¹ and A. R. Young²

1. *University of California, Los Alamos National Laboratory, Physics Division P-23, Los Alamos, NM 87545*

2. *North Carolina State University, Physics Department, Raleigh, NC 27695*

(Dated: November 6, 2018)

Spin waves, or magnons, in the anti-ferromagnetic α phase of solid oxygen provide a novel mechanism for ultra-cold neutron (UCN) production. Magnons dominate the energy exchange mechanisms for cold neutrons and UCN in solid α -oxygen, much in the same way as do phonons in solid deuterium superthermal UCN sources. We present calculations of UCN production and upscattering rates in S-O_2 . The results indicate that S-O_2 is potentially a much more efficient UCN source material than solid deuterium.

I. INTRODUCTION

Ultra-cold neutrons (UCN) provide a low energy system in which to carry out fundamental neutron physics experiments to a much higher degree of precision than that previously achieved with cold neutron experiments. UCN typically refer to neutrons with velocities less than 8 m/s. Potential experiments using UCN include the measurements of neutron β -decay parameters to test the Standard Model,^{1,2} the search for the neutron electric dipole moment to test time reversal symmetry,^{3,4} and the search for neutron-anti-neutron oscillations to test baryon number conservation.⁵ To date, some of these experiments have already been conducted with UCN but most of them are still statistically limited. To increase the UCN flux, Golub and Pendlebury⁶ proposed a “superthermal” source, in which the UCN production rate is enhanced through the efficient inelastic coupling of cold neutrons to the phonon modes of a condensed matter sample. The UCN loss rate is suppressed in these sources by the reduction of the thermal phonon population. Superthermal UCN sources have been successfully realized in super-fluid helium⁷ and solid deuterium.⁸ Here, we propose solid oxygen (S-O_2) as a superthermal source, which shows considerable promise for enhanced UCN production via a novel mechanism.

Solid α - $^{16}\text{O}_2$ has manifest magnetic properties. Its ability to interact with cold neutrons and UCN, through neutron-magnon inelastic scattering, provides potential advantages which stem from the energy dispersion spectrum of its anti-ferromagnetic magnons. The large neutron-magnon inelastic scattering rate together with oxygen’s small nuclear absorption cross section suggest that a S-O_2 UCN source may well compete favorably with solid deuterium UCN sources.

This report is organized as follows. In section II, we calculate the neutron-magnon and neutron-phonon scattering cross sections in solid oxygen, after reviewing the relevant magnetic properties and magnon dispersion relations. In section III we compare the predicted performance of a solid oxygen UCN source with the known performance of typical solid deuterium sources, and discuss possible mechanisms for UCN loss. We summarize our results in section IV.

II. NEUTRON-MAGNON SCATTERING

A. Magnetic Scattering Length

In solid oxygen at low temperatures ($T < 23.9\text{K}$), thermal fluctuations quench and long range anti-ferromagnetic ordering is established. This results from a slight distortion of the lattice structure from a rhombohedral (β phase) to a monoclinic symmetry (α phase). The resulting 2-D anti-ferromagnetic structure exhibits spin wave excitations.^{9,10} For our work on UCN, we will be concerned with S-O_2 in the α -phase below 10K, where superthermal UCN production is possible.

The magnetism of solid oxygen originates from the unpaired $2p$ electrons in the oxygen atom, two of which align and form a molecular ground state $^3\Sigma_g^-$ with a net spin $S = 1$ and an orbital angular momentum $l = 0$. For a diatomic molecule made of two ^{16}O atoms (naturally abundant), the null nuclear spin and antisymmetric electronic wave-function lead to a selection rule allowing only rotational states with odd parity.¹¹ The absence of half of the rotational states is an advantage in the application of S-O_2 as a UCN source, as will be discussed later.

A neutron interacts magnetically with an oxygen molecule. The interaction potential can be described as

$$V = \mu \cdot H = \mu \cdot \nabla \left(\frac{\mu_e \times R}{|R|^3} \right), \quad (1)$$

where $\mu = \gamma \mu_N \sigma$ is the neutron magnetic moment with neutron spin σ , and $\mu_e = -2\mu_B \hat{s}$ is the electron magnetic moment with electron spin \hat{s} . This magnetic coupling, which is the origin of neutron-magnon scattering, has an intrinsic scattering length of 5.4 fm.¹² This is comparable to typical neutron-nuclear scattering lengths, involved in neutron-phonon scatterings.

The differential cross section for neutron scattering in

the presence of the potential (1) can be written:

$$\begin{aligned} \frac{d^2\sigma}{d\Omega_f dE} &= \frac{k_f}{k_i} |\langle k_f \lambda_f | V | k_i \lambda_i \rangle|^2 \delta(\hbar\omega + E_{\lambda'} - E_{\lambda}) \\ &= \left(\frac{m_n}{2\pi\hbar^2}\right)^2 (2\gamma\mu_N\mu_B)^2 (4\pi)^2 \frac{k_f}{k_i} \sum_{\lambda_i \lambda_f \sigma_i \sigma_f} p_{\lambda_i} p_{\sigma_i} \\ &\quad \times |\langle \lambda_i \sigma_i | \hat{Q} | \lambda_f \sigma_f \rangle|^2 \delta(\hbar\omega + \Delta E) \\ &= r_0^2 \frac{k_f}{k_i} \mathbb{S}(\vec{\kappa}, \omega). \end{aligned} \quad (2)$$

Here \vec{k}_i is the initial neutron momentum vector, oriented relative to a crystal axis by a solid angle Ω_i , Ω_f is the solid angle for final neutron momentum k_f relative to the same crystal axis, and λ_i, λ_f are the initial and final states of the oxygen molecule. The above formula averages over the initial states of the target molecule and the neutron spin. From Eq.(1), the interaction matrix element is reduced to a scalar product between the neutron spin and the coherent lattice spin form factor \hat{Q} , which is defined using the neutron momentum transfer $\vec{\kappa} = \vec{k}_f - \vec{k}_i$ and the electron spin \hat{s}_i as

$$\hat{Q} = \sum_i e^{i\kappa \cdot r_i} \vec{\kappa} \times (\hat{s}_i \times \vec{\kappa}). \quad (3)$$

The differential cross-section is conventionally simplified as a product of the square of the scattering length, the kinematic factor $\frac{k_f}{k_i}$ and the scattering law $\mathbb{S}(\kappa, \omega)$.²⁵ The effective scattering length r_0 , characterizing the strength of magnetic neutron scattering, is given by

$$r_0 = \frac{m_n}{2\pi\hbar^2} \cdot 2\gamma\mu_N\mu_B \cdot 4\pi = \gamma \frac{e^2}{m_e c^2}, \quad (4)$$

where $\frac{e^2}{m_e c^2} = 2.82 \text{ fm}$ is the the classical electron radius and $\gamma = -1.91$ is the neutron gyro-magnetic ratio. The detailed physics of neutron interactions in solid O₂ is absorbed in the scattering law $\mathbb{S}(\kappa, \omega)$.

B. Anti-ferromagnetic Magnons in S-O₂

Calculation of the scattering law requires knowledge of the energy dispersion relation in the magnetic lattice of S-O₂. As shown in Fig.1, solid α -O₂ has a primitive unit cell with a distorted hexagon geometry.⁹ There are 14 oxygen molecules in the unit cell. On the basal plane, the b-axis is defined to be along the magnetization direction (which is also along one side of the hexagon), and the a-axis is assigned to be orthogonal to the b-axis. Due to a larger lattice constant along the c-axis, couplings between magnetization planes were found to be negligible compared to the in-plane couplings. The dominant 2-D magnetic structure are comprised of two interlacing sub-lattices, each carrying the opposite magnetization. Every lattice site is surrounded by 4 nearest neighbors on the opposite magnetic sub-lattice, and 2 next-nearest neighbors on the same magnetic sub-lattice.

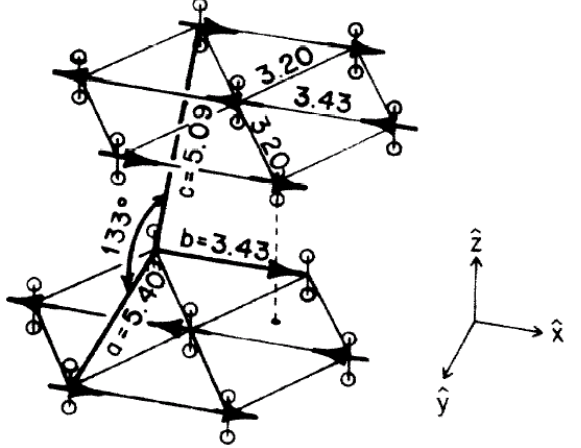


FIG. 1: A schematic of the lattice structure of solid α -O₂.⁹

This 2-D anti-ferromagnetic system can be described by the Heisenberg hamiltonian

$$H = -2 \sum_{\langle i,j \rangle} J_{ij} \mathbf{s}_i \cdot \mathbf{s}_j + \sum_i (-D s_{xi}^2 - D' s_{yi}^2 + D' s_{zi}^2), \quad (5)$$

where J_{ij} characterizes the strength of exchange interactions between molecular spin s_i on site i and s_j on site j . D represents the self-energy of the longitudinal spin, and D' the self-energy of the transverse spin (here, the b- and a-axes are parallel to the x and y-axes, respectively). Note that even though the out-of-plane coupling is weak, the self-energy term $D' s_z^2$ alone in the hamiltonian can result in significant contributions to scatterings in the z-direction.

The hamiltonian of Eq.(5) leads to the dispersion relation of magnon excitations⁹:

$$\omega_a(\vec{q}) = \sqrt{(2J_0 - 2J_{\vec{q}} - 2J'_0 + D)^2 - [2J'_{\vec{q}} + (-1)^a D']^2}. \quad (6)$$

Here $\omega_a(\vec{q}) \equiv \omega_{q,a}$ is the energy of a magnon, with momentum q . The angular dependence of the dispersion relation comes from $J_{\vec{q}}$ and $J'_{\vec{q}}$, which are the Fourier transform of the coupling coefficients J_{ij} : $J_{\vec{q}} = \sum_j J_{ij} e^{i\vec{q} \cdot \vec{r}_i}$ defined on the sites on one sub-lattice, and J' defined in the same way but on the opposite sub-lattice. Following the analysis of Stephens and Majkrzak,⁹ we take the numerical values of the spin coupling J_{NN} between the nearest neighbors to be -2.44 meV, the value J_{NNN} between the next nearest neighbors to be -1.22 meV, and J_{\perp} for the out-of-plane (z direction) coupling to be zero. Also, we use $D=0.132$ meV and $D'=0.118$ meV. Here, $a = \{0, 1\}$ is the branch index of magnon excitations, which include one acoustic and one optical mode.

Fig. 2 illustrates the dispersion relation at several different neutron scattering angles, together with the free neutron energy $E_n = \hbar^2 \kappa^2 / 2m_n$. For certain values of the incident neutron momentum, incident neutrons can

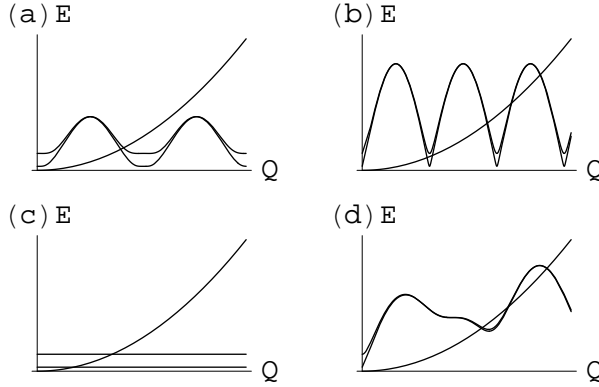


FIG. 2: The dispersion relation (Eq.(6)) of magnons in solid α -O₂ plotted for momentum transfer along (1,0,0) in (a), (0,1,0) in (b), (0,0,1) in (c), and (1,1,1) in (d). There are two branches (acoustic and optical). In (a,b,c) different periodicities originate from different lattice constants on these crystal axes. In (d), momentum transfers along a non-symmetry axis produce a non-periodic dispersion relation. Intersections with the parabolic free neutron dispersion set the four momentum (energy, momentum) for UCN production.

lose essentially all their kinetic energy in the excitation of single magnon, and emerge as (or “downscatter” to) UCN. These values are determined by the points where the free neutron curve intersects the magnon dispersion curves in Fig. 2. Note that this process is coherent, involving the simultaneous conservations of energy and momentum in the scattering process, and is analogous to the creation of UCN via phonon production in superfluid 4 He. We are only interested in the scattering conditions in which UCN are produced in the final state. Processes involving the creation of multiple magnons are also possible, but these are higher order effects which we expect to result in corrections on the level of a few percent and we neglect them in our calculation.

The energies of typical excitations in condensed matter systems range from tens to hundreds of Kelvin. This is comparable to the kinetic energy of cold neutrons. Cold neutrons are therefore used in UCN production experiments as they can efficiently couple to the condensed matter excitation modes and exploit the available energy exchange channels. Our goal is to transform as many incident cold neutrons into UCN as possible. Neutron downscattering through excitations in a bulk material is known to be the most efficient mechanism by far for this process.

In a solid target, the anisotropy of the lattice structure manifests itself in an orientation-dependent dispersion relation, as illustrated in Fig. 2. As a result, for every neutron momentum transfer κ , there exists a continuum of energy modes available for excitation. A large fraction of the incident cold neutron spectrum can therefore be used for UCN production. This is a potential advantage to the case of neutron scattering in super-fluid 4 He (the

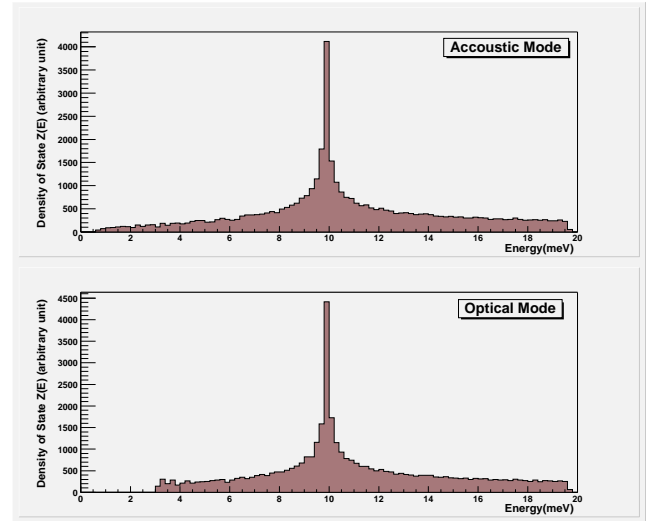


FIG. 3: The density of states of magnon excitation modes in solid α -O₂, dark histogram for the acoustic mode and light for the optical mode.

first proposed UCN source), where only a narrow band of incident neutrons with energy centered at 11 K can produce UCN. This results from the degenerate dispersion curves of phonon excitations in the super-fluid, which is an isotropic media.

When sampled uniformly over the 3-D magnon momentum space \vec{q} , the density of magnon states $Z(E)$ can be histogrammed over the energy scale, according to the allowed energy given by the dispersion relation Eq.(6), i.e.,

$$\sum_{\vec{q}} = \int dE Z(E). \quad (7)$$

The density of magnon states in S-O₂ is plotted in Fig. 3. A distinct peak at 10 meV results from the flattening of the dispersion curve approaching the Brillouin zone (BZ) boundaries of κ_x . One would also expect a 20 meV peak corresponding to the BZ boundary of κ_y , however, this peak is less significant because of the smaller flattening region due to the higher periodicity of κ_y . Note that there are no magnon modes with energies below $E_0 = 0.7$ meV. The absence of low energy magnon modes is particularly important for UCN upscattering events, and we will return to this point when discussing UCN loss in Sec. III.

C. Scattering Law in AFM crystals

The reference by Lovesey,¹² contains detailed calculations like the scattering matrix elements to the scattering law in Eq.(2). The scattering law for neutron inelastic scattering from a Heisenberg anti-ferromagnet with sin-

gle magnon creation(+) and annihilation(−) is given as

$$\begin{aligned} \mathbb{S}^{\pm}(\vec{\kappa}, \omega) &= [\frac{1}{2}gF(\kappa)]^2 \frac{1}{4}(1 + \tilde{k}_x^2)e^{-2W(\vec{\kappa})} \frac{(2\pi)^3}{Nv_0} \\ &\sum_{a=0,1} \sum_{q,\tau} (n + \frac{1}{2} \pm \frac{1}{2}) \delta(\hbar\omega_{q,a} \mp \hbar\omega) \delta^3(\vec{q} \mp \vec{\kappa} - \vec{\tau}) \\ &\times \{u_q^2 + v_q^2 + 2u_q \cdot v_q \cos(\vec{\rho} \cdot \vec{\tau})\}, \quad (8) \end{aligned}$$

where $F(\kappa)$ is the electron spin form factor of an oxygen molecule, $g = 2$ is the electron gyro-magnetic ratio, \tilde{k}_x is the unit neutron momentum vector projection on the magnetization direction, N is the total number of scatterers, v_0 is the unit volume occupied per scatterer, and n is the magnon occupation number. For the zeroth order approximation,¹⁴ we use the spherical Bessel function¹⁵ of order zero, $j_0(\kappa R/2)$, for the electron spin form factor $F(\kappa)$. The internuclear distance R is 1.21 Å.²⁶ The additional terms u_q and v_q are due to the two sets of spin waves in the opposite sublattices, and they can be reduced to

$$\begin{aligned} &\{u_q + (-1)^m v_q\}^2 \\ &= 2sN \frac{2J_0 - 2J'_0 - 2J_q + D - (-1)^m [2J'_q + (-1)^a D']}{E_a(q)}, \quad (9) \end{aligned}$$

with $m = 0$ for a nuclear peak, and $m = 1$ for a magnetic peak.

Summing over the allowed momentum transfer q , Eq.(8) can be further simplified to terms involving a discrete sum over allowed reciprocal lattice momentum τ :

$$\begin{aligned} &\frac{(2\pi)^3}{Nv_0} \sum_{q,\tau} \delta^3(\kappa + q - \tau) \\ &= \frac{(2\pi)^3}{Nv_0} \sum_{\tau} \frac{V}{(2\pi)^3} \int d^3q \delta^3(\kappa + q - \tau) = \sum_{\tau} \delta_{\tau,\kappa+q}. \quad (10) \end{aligned}$$

D. Evaluation of Neutron Coherent Scattering from Polycrystal

We are now ready to perform the cross-section calculations with the scattering law $\mathbb{S}(\kappa, \omega)$ for S-O₂. We present here our algorithm for calculating the pure coherent scattering cross-sections. We are interested only in the total cross-section which, according to Eq.(2), is

$$\sigma^{tot}(E_i, \Omega_i) = r_0^2 \int_0^{\infty} dE_f \int d\Omega_f \frac{k_f}{k_i} \mathbb{S}(\vec{\kappa}, \omega). \quad (11)$$

To consolidate the number of variables, we apply a coordinate transformation $(\Omega, E_f) \rightarrow (\vec{\kappa}, \omega) = (\phi, \kappa, \omega)$ with

$$\begin{cases} \omega = E_i - E_f \\ \kappa = \sqrt{k_f^2 + k_i^2 - 2k_f k_i \cos\theta} = \\ \sqrt{\frac{2m}{\hbar^2}} \sqrt{E_f + E_i - 2\sqrt{E_f E_i} \mu} \end{cases}$$

This leads to

$$d\Omega dE_f = (d\phi d\mu) dE_f = d\phi \left(\frac{\kappa}{k_f k_i} d\omega d\kappa \right). \quad (12)$$

Here, the neutron energy transfer ω is also the magnon energy gain, and κ represents the magnitude of neutron momentum transfer. The total scattering cross-section becomes

$$\sigma^{tot}(E_i, \Omega_i) = r_0^2 \int \int \int d\omega d\kappa d\phi \frac{\kappa}{k_f k_i} \frac{k_f}{k_i} \mathbb{S}(\vec{\kappa}, \omega), \quad (13)$$

which can be further reduced to

$$\sigma^{tot}(E_i) = 2\pi r_0^2 \frac{\hbar^2}{2mE_i} \int_{-E_{BZ}}^{\min(E_i, E_{BZ})} d\omega \int_{\kappa_{lower}}^{\kappa_{upper}} d\kappa \kappa \mathcal{S}(\kappa, \omega). \quad (14)$$

In a typical material with a periodic lattice structure, the dispersion relation contains the maximum energy at the Brillouin zone boundary, i.e., $\omega_{max} = E_{BZ}$. In the case of single magnon exchange, this defines the lower bound (energy gain) of the energy transfer integral. The upper bound (energy loss) can be up to E_{BZ} or the initial energy of the neutron. The lower, κ_{lower} , and upper, κ_{upper} , bounds in the momentum integral correspond to forward and backward scattering events, respectively: for a given magnitude of energy transfer and initial neutron energy,

$$\begin{aligned} \kappa^2 &\geq \frac{2m}{\hbar^2} (E_f + E_i - 2\sqrt{E_f E_i}) \equiv \kappa_{lower}^2 \\ \kappa^2 &\leq \frac{2m}{\hbar^2} (E_f + E_i + 2\sqrt{E_f E_i}) \equiv \kappa_{upper}^2. \quad (15) \end{aligned}$$

The bounds

$$|\kappa_{lower}| = \sqrt{\frac{2m}{\hbar^2}} \left| \sqrt{E_i - \omega} - \sqrt{E_i} \right| \quad (16)$$

$$|\kappa_{upper}| = \sqrt{\frac{2m}{\hbar^2}} (\sqrt{E_i - \omega} + \sqrt{E_i}) \quad (17)$$

are plotted, together with a contour plot of the scattering law, in Fig.4. The area bounded by these two curves defines the integration area.

Note that in the reduction Eq.(13) to Eq.(14), we have averaged the scattering law $\mathbb{S}(\vec{\kappa}, \omega)$ over the incident neutron angle Ω_i , i.e.,

$$\mathcal{S}(\kappa, \omega) = \frac{1}{4\pi} \int d\Omega_i \mathbb{S}(\vec{\kappa}, \omega). \quad (18)$$

The reduced scattering law, $\mathcal{S}(\kappa, \omega)$, is made isotropic, so that the double scalar variable integration in Eq.(14) becomes straightforward. Note that even though it results in the same form for the final integral, the treatment presented here does not make use of the “incoherent approximation” widely used in other cross-section calculation packages.¹⁶ The incoherent approximation relaxes the momentum conservation essential to coherent processes, and therefore it is subject to errors in the low

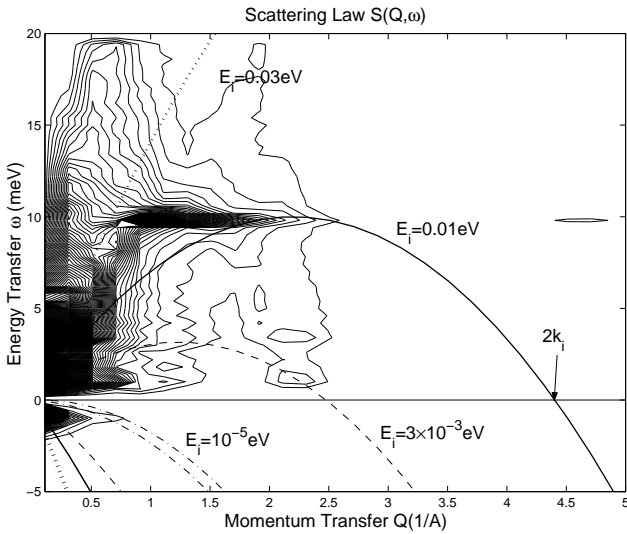


FIG. 4: A contour plot of the neutron scattering law $S(\kappa, \omega)$ in a 5 K solid α -O₂: The upper half plane ($\omega > 0 \rightarrow E_i > E_f$) covers neutron downscatterings, and the $\omega < 0$ covers neutron upscatterings. The area of integration is bounded by the dotted lines for incident neutrons with an initial energy $E_i = 0.03$ eV, and solid lines, dashed lines and dash-dotted lines, for $E_i = 0.01$ eV, 3×10^{-3} eV and 10^{-5} eV, respectively.

energy limit. Here, we arrive at Eq.(14) after integrating the scattering law $S(\vec{\kappa}, \omega)$ over the incident angle, and this is suitable for the case of neutron scattering off polycrystals.

Eq.(14) is evaluated numerically using a Monte-Carlo technique. We construct a table of values for the scattering law $S(\kappa, \omega)$ using the dispersion relation $\omega(\vec{\kappa})$ given in Eq.(6). With a given κ , the vector $\vec{\kappa} = (\kappa \sin \theta \cos \phi, \kappa \sin \theta \sin \phi, \kappa \cos \theta)$ is specified for a random choice of orientation angles (θ, ϕ) ; the dispersion relation $\omega(\vec{\kappa})$ gives the corresponding energy of excitation, ω . Momentum transfers larger than the BZ momentum are mapped back to the first BZ, according to Eq.(10), via unique Bloch translations. A numerical value of $S(\kappa_i, \omega_j)$ is then calculated and added to a running total for each bin (i, j) in the parameter space. This process is repeated, stepping through the parameter space according to $i\Delta\kappa = \kappa_i$ and $j\Delta\omega \leq \omega \leq (j+1)\Delta\omega$. Finally, we implement the angular average by repeating the Monte Carlo random angle assignment for each κ , and histogram the corresponding $S(\kappa, \omega)$ values.

Combining all the ideas above, we proceed to integrate Eq.(14) numerically by summing over all kinematically accessible points on a grid in the (ω, q) phase space. In the numerical approximation, the neutron downscatter-

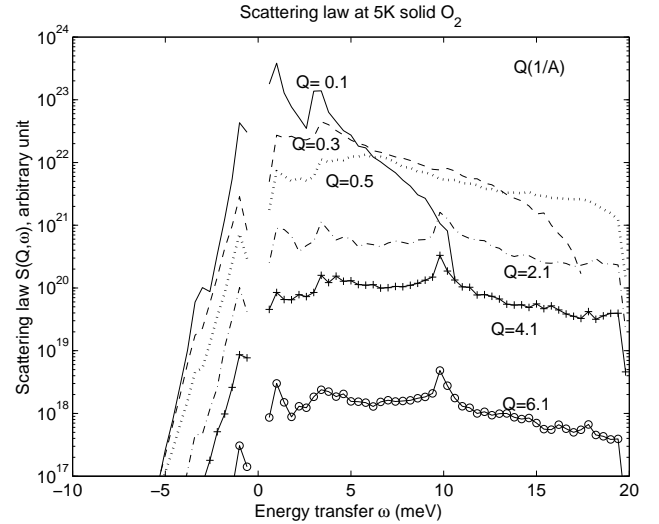


FIG. 5: Neutron scattering law $S(\kappa, \omega)$ in a 5 K solid α -O₂: $S(\kappa, \omega)$ is plotted as a function of energy transfer ω for momentum transfer $Q = 0.1, 0.3, 0.5, 2.1, 4.1$ and 6.1 \AA^{-1} . Distinct energy dependences are shown for $\omega > 0$ downscattering and $\omega < 0$ upscattering parts.

ing cross-section is given by

$$\sigma_{down}^{tot}(E_i) \cong 2\pi r_0^2 \frac{\hbar^2}{2mE_i} \sum_{l(\omega_l > 0)}^{l(\omega_l = \min(E_i, E_{BZ}))} \Delta\omega_l \times \sum_{m(\kappa_m = \kappa_{upper})}^{m(\kappa_m = \kappa_{lower})} \Delta\kappa_m \kappa_m S(\kappa_m, \omega_l) \quad (19)$$

and the upscattering cross-section is

$$\sigma_{up}^{tot}(E_i) \cong 2\pi r_0^2 \frac{\hbar^2}{2mE_i} \sum_{l(\omega_l > 0)}^{l(\omega_l = E_{BZ})} \Delta\omega_l \times \sum_{m(\kappa_m = \kappa_{upper})}^{m(\kappa_m = \kappa_{lower})} \Delta\kappa_m \kappa_m S(\kappa_m, -\omega_l). \quad (20)$$

For the results presented here, we constructed a table of $S(\kappa, \omega)$ values on a grid of 500×500 points, equally spaced by $\Delta\kappa = 0.02 \text{ \AA}$ and $\Delta\omega = 0.04 \text{ meV}$. The scattering law in a 5 K sample of solid oxygen is presented as a contour plot in Fig. 4, and the detailed dependence of $S(\kappa, \omega)$ on energy and momentum transfer is illustrated in Fig. 5. Notice that in both figures, at low κ , there exist two dominant contributions at 0.7 meV and 3 meV, which correspond to the self-energy terms involving D and D' of the acoustic and optical modes, respectively. As κ increases, the peak in the scattering law shifts to a higher value centered at 10 meV, which is clearly the BZ boundary energy, as discussed before.

Double integration of $S(\kappa, \omega)$ using Eq.(19) and Eq.(20) then produce the downscattering and upscattering cross sections for neutrons with a given initial energy.

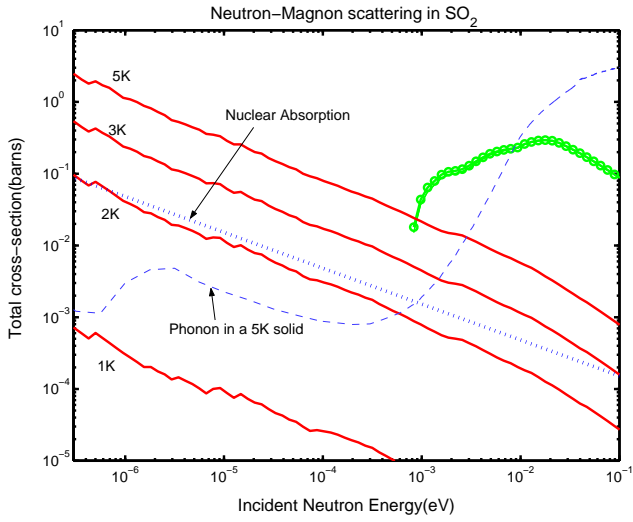


FIG. 6: Cross sections as a function of the incident neutron energy: Solid curves: neutron upscattering from solid α -O₂ at temperatures of 1 K, 2 K, 3 K and 5 K with annihilation of a single magnon. Circled curves: neutron downscattering via creation of one magnon from solid oxygen of 1 K, 2 K, 3 K and 5 K. Note that the downscattering cross section is nearly independent of the solid temperature. Dashed curve: neutron-phonon scattering in solid oxygen. Dotted curve: nuclear absorption cross-section per ¹⁶O₂ molecule.

The sum of the two gives the total cross sections. The resulting neutron-magnon scattering total cross sections in solid oxygen at various temperatures below E_0 are presented in Fig. 6.

E. Phonon Scattering in S-O₂

Neutron-phonon inelastic scattering is also present inside solid α -O₂. The scattering law for single phonon creation(+) and annihilation(−) is¹²

$$\mathbb{S}^{\pm}(\vec{\kappa}, \omega) = \frac{1}{2M_s} e^{-2W(\vec{\kappa})} \frac{(2\pi)^3}{v_0} \sum_{j=1,2,3} \sum_{q,\tau} \frac{|\vec{\kappa} \cdot \sigma^j(q)|^2}{\omega_j(q)} (n + \frac{1}{2} \pm \frac{1}{2}) \delta(\hbar\omega_{q,a} \mp \hbar\omega) \delta^3(\vec{q} \mp \vec{\kappa} - \vec{\tau}). \quad (21)$$

The neutron-phonon scattering cross-sections are calculated using LEAPR, one of the subroutines in the NJOY package developed in the Los Alamos National Laboratory.¹⁶ The incoherent approximation is used for the oxygen nucleus O¹⁶, even though it is a pure coherent scatterer. While we still expect a discrepancy at low energies, we expect the incoherent approximation to yield results differing from the actual phonon cross section by at most a small numerical factor¹³. An iterative expansion is used to include creation and annihilation of up to 100 phonons. The cross section for neutron-phonon

scattering is shown along with those for neutron-magnon scattering in Fig.6.

Note that the above formula is similar to Eq.(8), with the important distinction of an additional inverse dependence on the scatterer mass M_s . This indicates that phonon production is suppressed due to the smaller amplitudes associated with heavier nuclear recoil. Conversely, magnon excitation takes place via neutron-electron interactions, and thus does not have the mass suppression. To be more precise, we will compare the prefactors and the energy terms in Eq.(8) and Eq.(21) with the corresponding scattering length: for the magnon part, one finds

$$r_0^2 \left[\frac{1}{2} g F(\kappa) \right]^2 \frac{1}{4} (1 + \tilde{k}_x^2) \frac{O(4J_{NN})}{\omega_a(q)} \sim r_0^2 \times O(1) \times \frac{1}{3} \times \frac{10\text{meV}}{10\text{meV}};$$

for the phonon part, one has to pay attention to the detail that there are in fact two nuclei in one molecular scatterer, which contribute to the scattering amplitude coherently. Therefore, the relevant term is

$$(b + b)^2 \frac{1}{2M_s} \frac{|\vec{\kappa} \cdot \sigma^j(q)|^2}{\omega_j(q)} \sim 4b^2 \times \frac{1}{3} \times \frac{E_n}{\omega_{Debye}} \times \left(\frac{m_n}{M_s} \right) \sim 4b^2 \times \frac{1}{3} \times \frac{3\text{meV}}{10\text{meV}} \times \left(\frac{1}{2A} \right),$$

where A is the atomic number. As the intrinsic nuclear coherent scattering length ($b_c = 5.78$ fm for the ¹⁶O nucleus)¹⁷ is comparable to the magnetic scattering length ($r_0 = 5.4$ fm), the ratio of the neutron-phonon cross section to the neutron-magnon scattering cross section would naively be on the order of $1/A = 1/16$, assuming similar kinematics. The results of numerical integrations are presented in Fig.6, which show that the neutron-phonon scattering is overall weaker than the neutron-magnon scattering by about one order of magnitude for incident neutrons with energies less than 10 meV. This is consistent with the above analysis.

III. COMPARISONS OF PERFORMANCE BETWEEN S-O₂ AND S-D₂

A. UCN production

For the purpose of constructing a practical UCN source, we are interested not in the total cross section, but in the scattering events that cover the UCN phase space. To estimate the UCN production rate given a flux of incident neutrons with a broad spectrum, we carry out an integration of the differential cross section weighted by the cold neutron spectrum, i.e.,

$$P_{ucn} = n \int \left(\frac{d\sigma(E \rightarrow E_{ucn})}{dE} E_{ucn} \right) \Phi(E) dE, \quad (22)$$

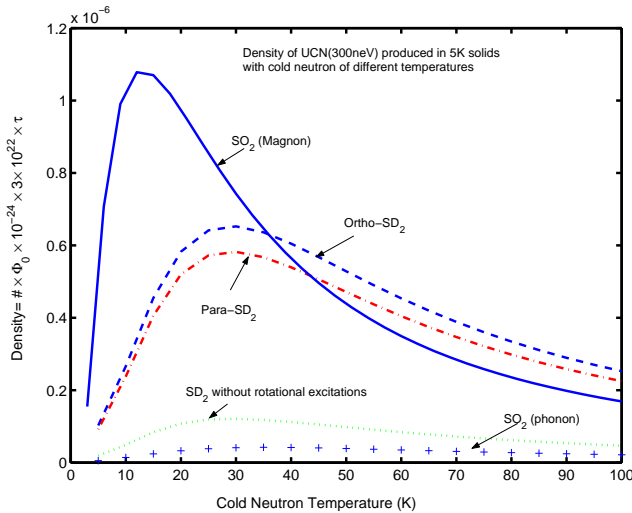


FIG. 7: UCN density vs. energy of the incident cold neutron flux characterized by the temperature a Maxwell-Boltzmann spectrum. The UCN production is optimum with a flux of 12 K cold neutrons in S-O₂, whereas it is optimum with a flux of 30 K cold neutrons in S-D₂.

where n is the density of the scatterers. We assume a Maxwell-Boltzmann energy distribution for the incident neutrons. The results are plotted in Fig.7 as a function of the incident cold neutron temperature. With a typical flux of 30 K cold neutrons on solid oxygen, we predict a UCN production rate of $2.2 \times 10^{-8}\Phi_0$, where Φ_0 is the total incident cold neutron flux. As shown in the plot, the optimum cold neutron temperature for UCN production in solid oxygen is about 12 K, which is roughly half the optimum cold neutron temperature for a S-D₂ source. This gives a UCN production rate of $P_{ucn} = 3.5 \times 10^{-8}\Phi_0$, a 60% improvement over the 30 K cold neutrons. For comparisons, the UCN production rates in S-D₂ are $1.95 \times 10^{-8}\Phi_0$ (in pure ortho S-D₂) and $1.74 \times 10^{-8}\Phi_0$ (in pure para S-D₂) with 30 K cold neutrons.

The maximum achievable UCN density is the production rate times the lifetime τ , i.e.,

$$\rho_{ucn} = P_{ucn} \times \tau. \quad (23)$$

For S-O₂ at 2 K, if there are no loss mechanisms other than nuclear absorption and magnon upscattering, $\tau = 375$ ms. By comparison, the longest lifetimes achievable in S-D₂ are approximately 40 ms,⁸ with the relative reduction due primarily to the larger nuclear absorption cross-section, hydrogen impurities and finite concentration of para-molecules. As a result, an improvement in UCN density of about an order of magnitude is expected in solid oxygen relative to solid deuterium.

Finally, the maximum achievable UCN flux is also determined by the fiducial source volume. For a solid deuterium source, the fiducial volume is limited by the incoherent elastic scattering length of 8 cm.⁸ In solid oxy-

gen, by contrast, the incoherent elastic scattering cross-section vanishes, so that the elastic mean free path is in principle infinite. Thus the fiducial volume of the solid oxygen source is expected to be limited solely by the neutron absorption length of 380 cm. Therefore, an improvement in source volume by a factor of up to

$$\left(\frac{380}{8}\right)^d \sim 50^d \quad d=1, 2, 3 \quad (24)$$

over solid deuterium is theoretically possible, though this will be limited by the maximum practical size of a solid cryogenic source. Here, d is the number of dimensions in which the source volume can expand. The tendency of micro-crystals to form in S-O₂,^{18,19} however, may limit the effectiveness of a large UCN source.

B. UCN loss

1. Thermal Upscattering

The 2-D symmetry of the AFM magnons in S-O₂ results in a fundamentally different dispersion curve from that of phonons. As it turns out, it takes a finite minimum energy E_0 of about 8 K to excite a magnon. For a solid oxygen sample of volume V with a temperature below 8K, the total number of magnons is given by

$$N = \sum_i n_i \cong \frac{V}{(2\pi)^3} \int_{E_0}^{\infty} Z(\epsilon) d\epsilon \left(\frac{1}{e^{\epsilon/k_B T} - 1} \right) \propto e^{-8K/T}. \quad (25)$$

That is, the number is exponentially suppressed as the solid cools.²⁷ For temperatures lower than 8 K, there are no low energy magnon levels available to be thermally populated, and only a small population of magnons with energy above E_0 exists. This results in a partial freeze-out of the UCN upscattering mechanism. The resulting exponential factor, $e^{-8K/T}$, of the magnon annihilation process results in a stronger temperature quenching effect on UCN upscattering than that of the typical phonon absorption mechanism. Note that the loss rate due to magnon upscattering is reduced to levels comparable to the nuclear absorption rate when the solid is cooled down to 2.1 K (see Fig. 6). This sets the operational temperature of a solid oxygen UCN source, as further cooling should increase the lifetime by no more than a factor of two.

2. Para-molecule Upscattering

Natural oxygen is over 99% ¹⁶O, which has a nuclear spin of zero. The molecular rotational spectrum has only one set of allowed states, and therefore ¹⁶O₂ molecules can not be left in long-lived rotational states at low temperature. The interaction of UCN with the rotational

states of D_2 , however, is a major source of loss in $S-D_2$ sources, and must be controlled by minimizing the para- D_2 concentration.^{20,21} UCN in $S-O_2$ are exempt from such a problem.

3. Losses specific to $S-O_2$

While nuclear absorption and magnon upscattering losses are theoretically well understood, this is not the case for the effects of polycrystal formation and various lattice defects. Previous experience with solid deuterium indicates that finite crystal effects do not introduce additional measurable scatterings, however, this statement might not apply to solid oxygen because of its very different thermal properties. This can only be answered by experiments.

In high radiation fields typical for neutron sources, ozone formation²² in oxygen solid may be a source of UCN loss, as the increase in mass fluctuations produces additional incoherent scatterings.²⁸ We also expect more γ -ray heating in oxygen because of its higher Z relative to solid deuterium. This, together with a lower thermal conductivity,²³ may increase the demand on cryogenic engineering to maintain the solid oxygen at 2 K. We have also estimated the effect of additional hyperfine transition energy in the $S-O_2$ crystal²⁴ on UCN loss. While we expect no significant rate of UCN upscattering from this mechanism, definitive measurements of the UCN lifetime in solid oxygen are required to place quantitative limits on this and other loss mechanisms.

IV. CONCLUSIONS

We have reviewed the potential of solid oxygen as a UCN source, by analyzing inelastic neutron-magnon scat-

tering. Oxygen appears to be a promising candidate, with strengths and weaknesses which complement those of solid deuterium.

The physics of UCN production in solid oxygen, involving magnon (spin wave) exchanges, is fundamentally different from the well-known phonon mechanism in solid deuterium. In solid oxygen, the neutrons are down-scattered through coupling to the magnons in the anti-ferromagnetic α -phase of the solid, the strength of which is comparable to the nuclear scattering (phonon) in solid deuterium. This mechanism has several advantages. For one, the absence of magnon states at low energy implies a greatly reduced UCN upscattering probability, relative to solid deuterium. Second, the smaller nuclear absorption cross-section of oxygen leads to a much longer UCN lifetime in this material. Also, the UCN loss due to the absorption of the excess energy from para-molecules (a major source of loss in solid deuterium) is absent in oxygen.

Preliminary calculations for solid oxygen indicate that the UCN density achievable should be about an order of magnitude greater than for solid deuterium. A factor of 10 gain in source volume should be readily feasible by taking advantage of the smaller neutron absorption probability and the infinite elastic scattering mean free path of UCN in solid oxygen. Together, these properties of solid oxygen suggest that a hundredfold increase in the UCN flux relative to what is available from solid deuterium should be possible, given the same incident neutron flux. The optimal operational temperature is 2 K, somewhat lower than that of solid deuterium (5 K).

¹ F. Glück, I. Joó and J. Lasts, Nuc. Phys. A **593**i 125 (1995).
² UCN collaboration, High precision measurement of the neutron spin-electron correlation asymmetry in neutron β -decay using ultra-cold neutrons. (<http://lanl-db1.lanl.gov/UCN/ucnbetaasymmetrylb.nsf>)
³ I.B. Khriplovich and S.K. Lamoreaux, *CP Violation Without Strangeness: Electrical Dipole Moments of Particles, Atoms and Molecules* (Springer, New York, 1997).
⁴ N.F. Ramsey, *In Discovery of Weak Neutral Currents: The Weak Interaction Before and After*, eds. A.K. Mann, D.B. Cline (AIP, New York 1993); N.F. Ramsey, Phys. Rev. **109**, 222 (1958).
⁵ Y. Kamyshkov, Surv. High Energy Phys. **13**, No. 1-3, 2 (1998).
⁶ R. Golub and J.M. Pendlebury, Phys. Lett., **53A**, 133 (1975).
⁷ P. Ageron, W. Mampe, R. Golub and J. M. Pendlebury, Phys. Lett. **66A** 469 (1978).
⁸ C. Morris *et al.*, Phys. Rev. Lett. **89**, 272501 (2002).
⁹ P. W. Stephens and C. F. Majkrzak, Phys. Rev. B **33**, 1 (1986).
¹⁰ I. N. Krupskii, A. I. Prokhvatilov, Yu. A. Freiman and A. I. Frenburg, Fiz. Nizk. Temp. **5**, 271 (1979) [Sov. J. Low Temp. Phys. **5**, 130 (1979)].
¹¹ A. Compaan and A. Wagoner, Am. J. Phys., **62** (7), 639 (1994).
¹² S. W. Lovesey, *Theory of neutron scattering from condensed matter* (Clarendon press, Oxford, 1984), Vol II, ch. 4.
¹³ C.-Y. Liu, doctoral dissertation, physics, Princeton University, 2002 (unpublished).
¹⁴ W. H. Kleiner, Phys. Rev. **97**, No. 2, 411 (1955).
¹⁵ N.M. Temme, *Special functions – An introduction to the classical functions of mathematical physics* (John Wiley & Sons, New York, 1996), 399.
¹⁶ R. MacFarlane, Technical Report No. LA-12639-MS (ENDF-356), Los Alamos National Laboratory, Los

Alamos, NM (March, 1994).

¹⁷ V. F. Sears, *Neutron optics: an introduction to the theory of neutron optical phenomena and their applications* (Oxford University Press, New York, 1989).

¹⁸ Giauque and Johnston, J. Am. Chem. Soc. **51**, 2300 (1929).

¹⁹ Fagerstroem and Hallet, JLTP **1**, 3 (1969).

²⁰ C.-Y. Liu, A. R. Young and S. K. Lamoreaux, Phys. Rev. B **62**, R3581 (2000).

²¹ C.-Y. Liu *et al.*, Nucl. Instr. Meth. A **508**, 257 (2003).

²² Baragiola, *et al.*, Nucl. Instr. Meth. B **157**, 233 (1999).

²³ A. Jezowski, P. Stachowiak, V. V. Sumarokov, and J. Mucha, Phys. Rev. Lett. **71**, 97 (1993).

²⁴ E. J. Wachtel and R. G. Wheeler, J. Appl. Phys. **42**, 1581 (1971).

²⁵ The scattering law $S(\kappa, \omega)$ defined here is slightly different from that defined in Ref⁹ which only retains the dynamical structure factor.

²⁶ Although difficult to quantify, we believe that our calculations are accurate within a factor of 2.

²⁷ In the above estimation, we approximate the density of states, $Z(\epsilon)$, to be roughly constant above E_0 .

²⁸ Ozone may also be a safety concern, although the risk is greatly reduced in the proposed experiment using a spallation neutron source which has a small radiation background.